Available online at www.sciencedirect.com
ScienceDirect
Trans. Nonferrous Met. Soc. China 29(2019) 2483−2495
Transactions of Nonferrous Metals Society of China
www.tnmsc.cn

Parametric optimization and microstructural characterization of friction welded aeronautic aluminum alloy 2024

Pei-hao GENG[1,2], Guo-liang QIN[1,2], Jun ZHOU[3], Chang-an LI[1,2]

1. Key Laboratory for Liquid−Solid Structure Evolution and Processing of Materials, Ministry of Education, Shandong University, Ji'nan 250061, China;
2. Institute of Materials Joining, Shandong University, Ji'nan 250061, China;
3. Harbin Welding Institute, Chinese Academy of Machinery Science and Technology, Harbin 150028, China

Received 25 February 2019; accepted 16 July 2019

Abstract: Continuous drive friction welding was employed to join the aeronautic aluminum alloy 2024. Parametric optimization and microstructural characterization were investigated. Results show that friction pressure is the most significant factor influencing the tensile strength of joints. To obtain a high joint efficiency, the combination of moderate friction pressure, less friction time and higher upset pressure is recommended. The optimized joint efficiency from Taguchi analysis reaches 92% of base metal. Under the optimized experimental condition, the interfacial peak temperature is calculated analytically in the range of 779−794 K, which is validated by experimental data. Fine recrystallized grains caused by the high temperature and plastic deformation are observed in the friction interface zone. The grain refinement is limited in the thermo-mechanically affected zone, where most of matrix grains are deformed severely. The extensive dissolution and limited re-precipitation of strengthening phases result in a lower microhardness in the friction interface zone than that in the thermo-mechanically affected zone.

Key words: AA2024 alloy; continuous drive friction welding; Taguchi analysis; microstructure evolution; mechanical properties

1 Introduction

The aeronautical grade aluminum alloy 2024 (AA2024), as an age-hardenable alloy, has been increasingly used in the fabrication of light weight structures, owing to its high specific strength, excellent corrosion resistance and good fracture toughness [1]. Excellent mechanical properties can be attributed to the precipitation of strengthening phases, such as Al_2Cu (θ) and Al_2CuMg (S) upon solid solution and artificial aging [2]. To join the aluminum alloy, the conventional fusion welding usually results in the dissolution and growth of strengthening precipitates in the weld during the thermal cycle. It is difficult to obtain a sound welded joint owing to the occurrence of solidification cracks, coarse grain porosities, and slag inclusions in the fusion welding of aluminum alloys [3−5]. In contrast, owing to the technical advantages of solid-state welding such as refined microstructure and no solidification, friction welding techniques such as rotational friction welding (RFW), friction stir welding (FSW) and linear friction welding (LFW) have been introduced and used to join the various aluminum alloys [6]. These three friction welding techniques have been used to weld the axisymmetric, the plate-shaped, and the non-axisymmetric workpieces, respectively. As the most conventional friction welding, RFW is the emphasis of this study. RFW is quite suitable to join the axisymmetric workpieces. During process, one workpiece is rotated and in contact with another workpiece under the axial force. Heat generated by friction between two contact workpieces softens the interfacial materials, and simultaneously hot plasticized materials are extruded out from interface. There are two mainly driving modes of workpiece rotation [7]. One is the continuous driving mode, which means that the rotation maintains at the constant speed, and another one is the inertial driving mode, which is implemented by a rotational flywheel with rotational inertia. Once the required burn-off is

Foundation item: Project (51475196) supported by the National Natural Science Foundation of China; Project (2017ZX04004001) supported by the National Science and Technology Major Project on High-end Numerically Controlled Machine Tools and Basic Manufacturing Technology, China

Corresponding author: Guo-liang QIN; Tel: +86-13505400905; E-mail: glqin@sdu.edu.cn

DOI: 10.1016/S1003-6326(19)65156-3

reached, or the rotation speed decreases to a certain value, a forged force will be applied on the stationary workpiece and maintained to consolidate a sound joint.

To date, it is reported that RFW has been successfully welded the various aluminum alloys. LIENERT et al [8] reported that the inertia friction weld could effectively join the SiC-reinforced aluminum alloys with little loss in hardness and tensile properties. KIMURA et al [9] described the effects of friction welding conditions on joining phenomena during the friction stage, after lucubrating the friction torque changing curve. They also concluded that the joining mechanism of AA7075 friction welding was similar to that of low carbon steel. Also, KIMURA et al [10] investigated the optimized process parameters during the AA5052 friction welding. The joint which existed in the soften region at the periphery, had approximately 93% joint efficiency and fractured in base metal (BM). RAFI et al [11] identified the optimum combination of process parameters in RFW of AA7075 by designing experimental parameters. Recently, YAMAMOTO et al [12] found that the fatigue limit of sound friction welded joints of AA6061 was slightly lower than that of BM. All joints fractured in heat affected zone (HAZ). SAHIN et al [13] found that the refining of grain size resulted in a significant increase in hardness and mechanical properties of friction welded near-nanostructured AA5086. In addition, some authors aimed to optimize the welding parameters in RFW of aluminum alloys using numerical simulation. DONATI et al [14] investigated the thermal field in RFW of AA6082, which was used for analysis of welding quality. SINGH et al [15,16] reported the weld ability of semi-solid processed aluminum alloys via high temperature flow behavior in RFW. The tensile strength of joint was higher than that of BM. DARSIN et al [17] found that a long friction time resulted in the soften in the weld zone of friction welded 6xxx series aluminum alloy. Recently, RFW for pipe of aluminum alloy was studied by WANG et al [18]. DAI et al [19] found that the heat input had an evident impact on the joint appearance in RFW of spray forming AA7055.

To the author's knowledge, there has not been published available information on RFW of AA2024, and the corresponding microstructure evolution in the weld. Therefore, the joint of AA2024 is produced by the continuous driving friction welding (CDFW) in this study, which is hoped to fill the scarcity on the RFW of aluminum alloys. One of the objectives is to optimize the welding parameters to improve weld strength of the continuous driving friction welded (CDFWed) joints of AA2024 by utilizing the design of experiments (DoE). The other is to investigate the microstructural evolution and its influence on properties. In this study, the Taguchi L9 orthogonal array and analysis of variance (ANOVA) are used to systematically investigate the effects of welding parameters on process. The microstructure is examined by the optical microscopy (OM), and scanning electron microscope (SEM) with energy dispersive X-ray spectroscopy (EDS). Additionally, the peak temperature in the weld zone is studied analytically.

2 Experimental

2.1 Welded materials

The as-rolled AA2024 bars with 12 mm in diameter and 60 mm in length were used in this study. The actual chemical composition of the BM was determined using the optical emission spectrometry (OES) as listed in Table 1. The OM image of AA2024 is shown in Fig. 1. Some deformed α-Al matrix grains can be observed. The average size of matrix grain is approximately (8±2) μm. Moreover, the block or rounded-shaped particles precipitate around the grain boundary along the rolled direction. These particles such as Al_2Cu (θ) or Al_2CuMg (S) precipitation provide the high strength and hardness for the α-Al matrix.

2.2 Continuous drive friction welding

A PC-controlled CDFW machine was used to join the AA2024 bars. Welding parameters such as friction pressure (P_f), friction time (t_f) and upset pressure (P_u) can be controlled precisely and rotational velocity is kept constant at 2200 r/min. Before welding operations, the contact surface of workpieces has been polished and cleaned by acetone. The schematic of the RFW of aluminum alloy bars is presented in Fig. 2. To obtain a sound joint with high joint strength, the welding parameters varied in large ranges, which are friction pressure of 20−60 MPa, friction time of 4−12 s, and upset pressure of 70−110 MPa, respectively. In-process temperature in joint made by optimal welding parameters was recorded. As shown in Fig. 2, the thermal cycles at different initial positions from friction interface (i.e. 2.5, 3.5, 5 and 6.5 mm) were measured by an array of K-type thermocouples.

Table 1 Chemical composition and mechanical properties of AA2024

Measured chemical composition/wt.%							Tensile strength/MPa	Microhardness ($HV_{0.5}$)
Si	Fe	Cu	Mg	Mn	Zn	Al		
0.5	0.2	4.5	1.5	0.6	0.3	Bal.	502	120

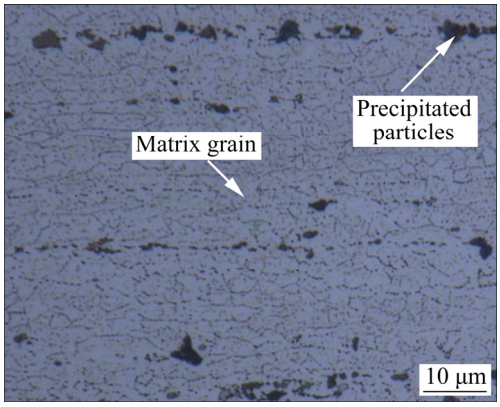

Fig. 1 OM image of AA2024

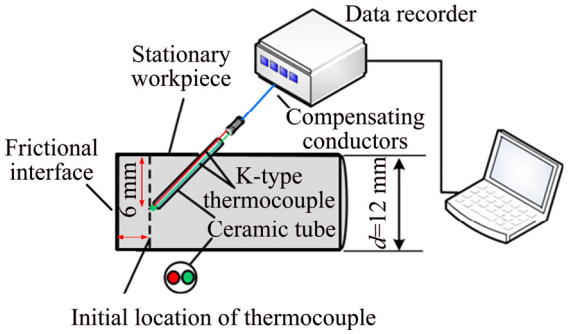

Fig. 2 Schematic of RFW of aluminum alloy bars with preset thermocouple

2.3 Taguchi experimental design

To investigate the effects of welding parameters on joint strength, the Taguchi analysis, as an efficient DoE method, could improve the performance of the product, process and system with a significant slash in experimental time and cost [20]. Three categories of quality characteristics are defined in the signal/noise analysis (S/N ratio), i.e. the larger-the-better, the nominal-the-better and the lower-the-better [21]. In this experimental process, the joint efficiency, which is the ratio of tensile strength of welded joints to that of the BM, is considered as the response. To maximize the response, the S/N ratio (ϕ_j) was chosen according to the category of "the larger-the-better", and can be expressed as

$$\phi_j = -10\lg\left(\frac{1}{n}\sum Y_{ij}^2\right) \quad (1)$$

where Y_{ij} is the value of the ith quality characteristics in the jth experiment, and n is the number of the experiments. To simplify the investigation and consider the actual situations, the Taguchi L9 orthogonal array was selected for evaluation of the effects of three welding parameters. Three specimens are prepared at each experimental level. Table 2 shows the experimental layout of L9 orthogonal array factors and levels. In addition, the ANOVA has been carried out to evaluate the effect significance of welding parameters. The contribution of each process parameter to response was also calculated using ANOVA method.

Table 2 Experimental parameters of Taguchi L9 orthogonal array

Level	P_f/MPa	P_u/MPa	t_f/s
1	20	70	4
2	40	90	8
3	60	110	12

2.4 Mechanical properties and microstructure examination

Tensile tests are carried out in a 100 kN electro-mechanically controlled universal testing machine (SANS, WDW−100D) under an engineering strain rate of 0.0005 s^{-1} at room temperature. It is noted to mention that all tensile tests are conducted within one day after welding, which is as far as possible to avoid the natural aging. Figure 3 shows the schematic of dimensions of tensile sample. Cross-sectional samples for micro-structural examination were prepared following the standard metallographic procedures. Specimens were polished and etched using the Keller's reagent. The OM and SEM with energy dispersive X-ray spectroscopy were used to examine the microstructure for the nine welded samples. Besides, fracture morphology of joint at optimal welding parameters was also observed. Micro-hardness measurements in the weld were performed using a load of 4.9 N, applied for 15 s. Measurements

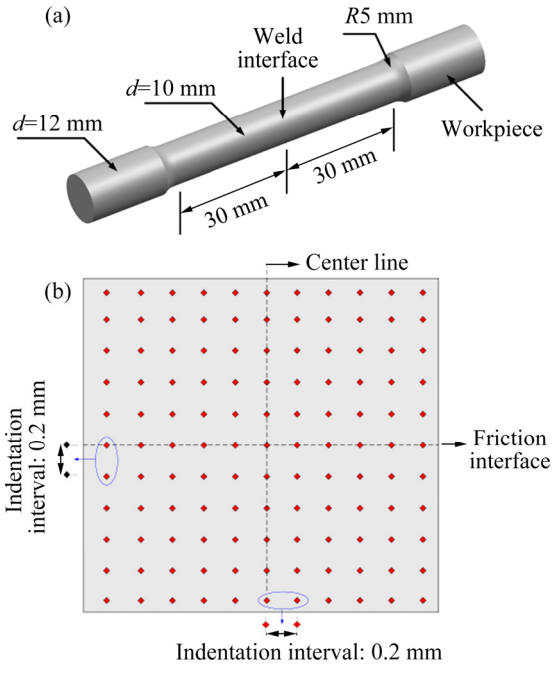

Fig. 3 Schematic of dimensions of tensile samples (a) and indentation locations used for hardness measurement (b)

were carried out from the friction interface to the base metal zone on the cross-sectional surface and the indentation locations is schematically shown in Fig. 3(b). The constant indentation interval of 0.2 mm was used in the measurements

3 Results and discussion

3.1 Optimization of welding parameters

Table 4 shows the results of response for each welding parameter combination in Taguchi L9 orthogonal array. It is clearly seen that the joint strength of all joints is lower than that of the BM. Among the experimental joints, the maximum joint efficiency is approximately 88%, which is obtained at P_f =40 MPa, t_f=12 s, and P_u=90 MPa. The minimum joint efficiency is approximately 29%, which is obtained at P_f =20 MPa, t_f=4 s, and P_u=70 MPa. It is well known that the RFW is divided into two distinct stages: friction stage and upset stage. As stated by LI et al [22], the plastic flow occurred at high temperatures caused by sufficient heat at the interface. As the rotation speed is constant, heat input into the joints is dependent on the friction pressure and heat time. In this study, the lowest weld strength at P_f=20 MPa, t_f=4 s, and P_u=70 MPa can be attributed to the insufficient friction heat input at the interface caused by low friction pressures. Compared to the joint at P_f= 20 MPa, t_f=4 s, and P_u=70 MPa, the tensile strength of joint at P_f=20 MPa, t_f=12 s, and P_u=110 MPa achieved 76%. This indicates that a sufficient friction time is also important to improve the joint efficiency. A sufficient quantity of heat could not be produced for welding at low friction time. However, as a sufficient heat is achieved at high friction pressure, the increasing friction time is not desired to obtain a sound joint for aluminum alloy owing to the occurrence of the softening of weld zone. For example, a low joint efficiency is found at P_f=60 MPa, t_f=12 s, and P_u=70 MPa. Excessive heat inputs under long heating time may coarsen the refined grains at the interface or near region and then result in the deterioration of joint properties. As the process reaches the upset stage, the plastic metals are extruded out subsequently under higher upset pressures. When comparing the joint efficiency of joint at P_f=60 MPa, t_f=12 s, and P_u=70 MPa to that at P_f=20 MPa, t_f=12 s, and P_u=110 MPa, the joint efficiency increases from 53% to 76%. The further extrusion under suitable upset pressure can consolidate the uniformity of thermo-mechanical coupled region. The plastic deformation zone will be narrowed, which can improve the joint efficiency.

Table 3 Orthogonal array for L9 with response (raw data)

Sample No.	P_f/ MPa	P_u/ MPa	t_f/ s	Joint efficiency/%			
				R_1	R_2	R_3	Average
1	20	70	4	25.7	27.89	32.67	28.75
2	40	70	8	86.45	83.86	82.27	84.20
3	60	70	12	52.19	54.18	52.39	52.92
4	20	90	8	48.80	53.39	57.17	53.12
5	40	90	12	91.43	86.25	86.65	88.11
6	60	90	4	71.12	72.51	76.69	73.44
7	20	110	12	76.69	76.69	73.31	75.56
8	40	110	4	70.72	75.50	71.51	72.58
9	60	110	8	87.85	90.64	83.86	87.45

R_1, R_2 and R_3 represent the raw data of three duplicate trails

3.1.1 Analysis of variance

The experimental results are transformed into mean and S/N ratio, which are used to assess the influence of process parameters on the response. Table 4 lists the mean and S/N ratio calculated for each parameter at three levels. The values in the last row of Table 4 mean rank, which help to assess which parameter has the greatest effect on the response. The order of importance of the welding parameters for two main effects is: friction pressure > upset pressure> friction time (Table 4). The greatest variations of both mean joint efficiency and S/N ratio are observed for friction pressure, revealing that this welding parameter has the most important influence on the joint efficiency. Upset pressure has a lower relevant influence and friction time shows the lowest influence of all welding parameters.

Table 4 Main effects of welding parameters on joint efficiency (mean and S/N ratio)

Level	Mean/%			S/N ratio		
	P_f	P_u	t_f	P_f	P_u	t_f
1	52.67	55.00	58.33	33.78	34.04	34.59
2	81.00	71.67	74.33	38.14	36.92	37.22
3	71.33	78.33	72.33	36.89	37.85	37.00
Difference	28.33	23.33	16.00	4.36	3.81	2.63
Rank	1	2	3	1	2	3

The comparison of mean effect and S/N ratios of joint efficiency is shown in Fig. 4. In the investigated range, the plot of upset pressure suggests an increase in this parameter to obtain joints with a higher strength, while the plots of friction pressure and friction time indicate a slight reduction in the joint efficiency above the intermediate levels. According to the analysis above, the optimal welding parameter level combinations are the 2th level friction pressure, the 3rd level upset pressure and the 2th level friction time.

The ANOVA is performed to investigate the importance of each welding parameter in terms of variance and contribution on joint efficiency. Tables 5 and 6 list the ANOVA results for joint efficiency of mean

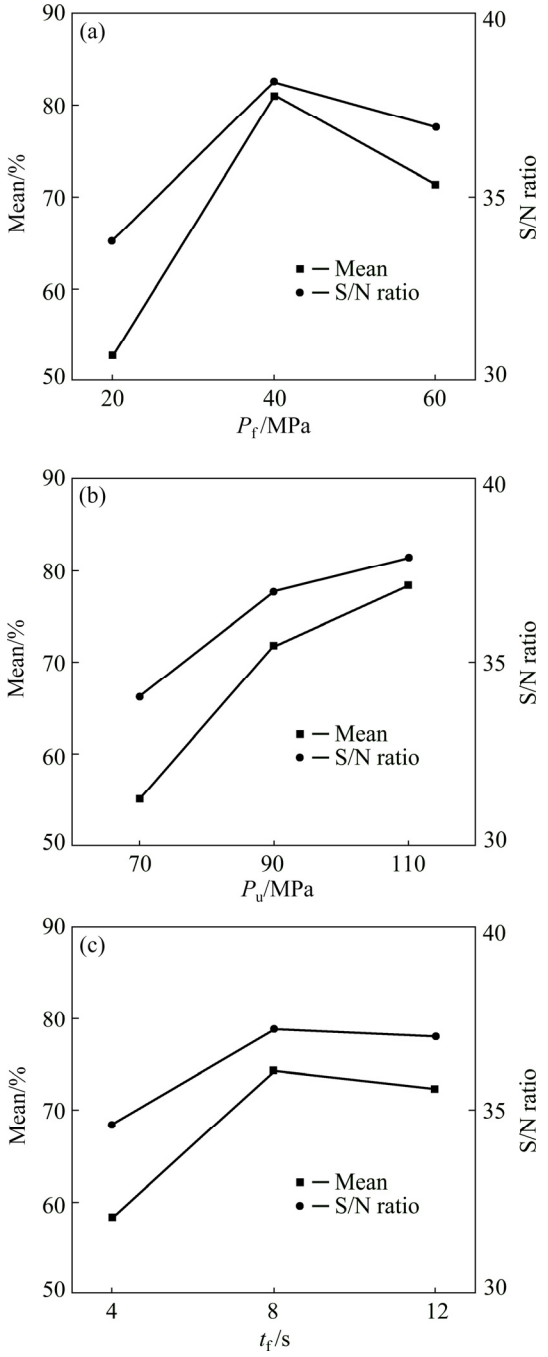

Fig. 4 Comparison of mean and S/N ratio of joint efficiency: (a) P_f; (b) P_u; (c) t_f

and S/N ratio, respectively. Herein, the F>3.5 means that the change of the design parameters has a significant effect on the quality characteristic. The results indicate that the studied welding parameters are highly significant factors influencing the joint efficiency in the order of friction pressure, upset pressure and friction time. Moreover, friction pressure has the highest contribution both in terms of mean and S/N ratio. However, the contribution of friction time is less than that of total error contribution, indicating that friction time contributes least to the joint efficiency.

Table 5 ANOVA results of mean joint efficiency

Source	Degree of freedom	Sum of square	Mean square	F	Contribution/ %
P_f	2	3930	1965	23.96	39.35
P_u	2	2560	1280	15.61	25.04
t_f	2	1439	719.5	8.11	13.32
Error	20	1641	82.05		22.29
Total	26	9570			100.0

Table 6 ANOVA results of S/N ratio for joint efficiency

Source	Degree of freedom	Sum of square	Mean square	F	Contribution/ %
P_f	2	23.7877	11.8939	26.47	40.67
P_u	2	17.8849	8.9425	19.9	27.99
t_f	2	10.0361	5.0181	11.17	15.05
Error	20	8.9865	0.4493		16.29
Total	26	60.6953			100.0

According to the statistical analysis, the understanding of the effects of welding parameters on the tensile strength of CDFWed AA2024 joints can be obtained. In this investigated experimental range, friction pressure becomes a crucial controlled factor in the CDFW of AA2024, which plays a dominant role in obtaining high heat efficiency at interface. As a result, plastic deformation occurs in a short time, accompanied with increasing axial shortening length. In addition, a suitable friction time is also important. In particular, too sufficient friction time will be detrimental to improve the joint efficiency due to the coarse grains and strengthening phase caused by extensive heat. A higher upset pressure can usually improve the joint efficiency, which can be attributed to the more uniform interfacial microstructure and narrower plastic deformation zone. Therefore, when welding AA2024 as well as other hard Al alloys, moderate friction pressure (40 MPa) with higher upset pressure (90−110 MPa) is considered to be more favorable to improve joint efficiency. Meanwhile, friction time can be selected at the low level (4−8 s) as it will be beneficial for minimizing the overall axial reduction and material wastage, and improving processing efficiency.

3.1.2 Confirmation tests

The obtained optimal parameter combination is P_f=40 MPa, P_u=110 MPa and t_f=8 s, which is not among the original design combinations. This is related to the multifactor nature of the Taguchi experiment design employed. The optimum joint efficiency was predicted at the significant levels of crucial parameters. Based on the ANOVA and contribution analysis, the selected factors are all significantly high. However, the contribution

indicates that the friction pressure and upset pressure are the crucial factors. Similar results are obtained by LAKSHMINARAYANAN and BALASUBRAMANIAN [23] and VIJIAN and ARUNACHALAM [24] on optimization of process parameters using Taguchi analysis. The optimal joint efficiency can be predicted at the significant levels of significant parameters. Hence, the estimated mean of the response joint efficiency can be expressed as

$$\lambda = \overline{P_{f2}} + \overline{P_{u3}} - \bar{M} \quad (2)$$

where λ is joint efficiency, $\overline{P_{f2}}$ is the average joint efficiency at the second level of friction pressure, 40 MPa; $\overline{P_{u3}}$ is the average joint efficiency at the third level of upset pressure, 110 MPa; $\bar{M}$ is the average joint efficiency of all levels of three welding parameters. Substituting the values of various terms in Eq. (2), then,

$$\lambda=81.63\%+78.53\%-68.46\%=91.70\% \quad (3)$$

Three confirmation validated experiments are conducted using the optimal parameters to verify the improvement in joint efficiency. The friction pressure, upset pressure and friction time are set to be 40 MPa, 110 MPa and 8 s, respectively. The average joint efficiency of friction welded AA2024 is found to be 92.03%, which is quite close to the predicted optimal joint efficiency.

3.2 Characterization of weld microstructure

3.2.1 Temperature measurement in weld zone

In consideration of the significant influence of high temperature on the microstructure, the thermal cycles during the CDFW of AA2024 at optimal welding parameters were measured in this study. As shown in Fig. 5, thermal cycles show that materials at different distances from interface experience different heating and cooling rates. A larger heating rate exists in the region closer to interface. In this study, an initial heat rate of (96±31) K/s is recorded at the initial distance of 2.5 mm from the interface, which indicates that a very sharp temperature rise is observed in the weld region owing to the nature of process. However, as the friction time exceeds 5 s, it is found that the slope of thermal profile at the initial distance of 2.5 mm decreases. This may be due to the fact that the thermal equilibrium is reached at the friction interface. It is also found that the temperature at the initial distance of 2.5 mm shows a rapid increase when the process reaches the upset stage. To consolidate the bonding, two AA2024 bars are held together under upset pressure of 110 MPa, which is higher than friction pressure of 40 MPa. This results in the further increase of axial shortening from 3.5 to 4.6 mm in a short time at upset stage. At the beginning of this stage, a modest temperature increase from 753 to 776 K can be observed

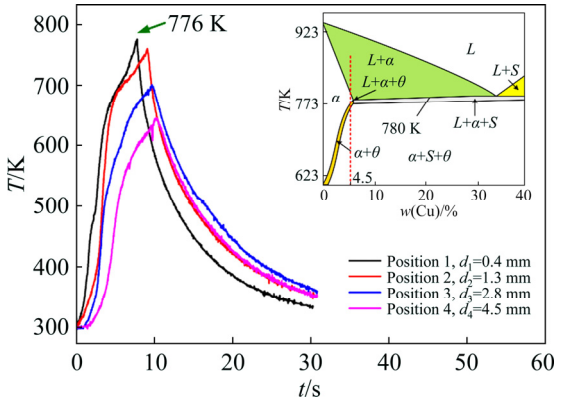

Fig. 5 Temperature profiles at various locations from interface during welding process

owing to the adiabatic heating from plastic deformation work of the materials. As reported, the adiabatic heating has a significant effect on the temperature rise under higher strain rates. GOTEZ and SEMIATIN [25] proposed an analytical equation to calculate the temperature increase (ΔT) during deformation, which is expressed as

$$\Delta T = 0.95\eta\int \sigma \mathrm{d}\varepsilon/(\rho c_p) \quad (4)$$

where η is the adiabatic correction factor, $\int \sigma \mathrm{d}\varepsilon$ is the area under the uncorrected stress−strain curve, ρ is the density, and c_p is the specific heat capacity. The factor of 0.95 is the fraction of mechanical work transformed to heat. The values for ρ and c_p are 2700 kg/m^3, and 1100 J/(kg·K) for AA2024, respectively [26]. The η has typically been taken to vary linearly with $\lg \dot{\varepsilon}$ [27], i.e. η values are equal to 0.0, 0.25, 0.5, 0.75, and 1.0 for strain rates of 0.001, 0.01, 0.1, 1, and 10, respectively. The steady state flow stress of AA2024 is described as [28]

$$\sigma = \frac{1}{\alpha_0}\ln\left\{\left(\frac{Z}{A}\right)^{1/n} + \left[1+\left(\frac{Z}{A}\right)^{2/n}\right]^{1/2}\right\} \quad (5)$$

where the Zener−Hollomon parameter Z is given by

$$Z = \dot{\varepsilon}\exp\left(\frac{Q}{RT}\right) \quad (6)$$

where the material parameters of α_0, n, Q, and $\ln A$ are 0.016 MPa^{-1}, 427, 149 kJ/mol, and 19.6 s^{-1}, respectively, and R is the gas constant. In fact, the strain rate should be known to determine the flow stress at the temperature of 753 K. As studied by GRANT et al [29], it was reasonable to assume that the steady state strain rate could reach the magnitude from 10^{-1} to 10^{1} s^{-1}. Therefore, according to Eqs. (4) to (6), the calculated change in temperature is 10−24 K, indicating a good agreement between the analytical and observed values.

Thus, it is reasonable to presume that the temperature increase at the beginning of upset stage is due to plastic deformation work. In addition, the cooling rates at four distances are calculated as nearly 105, 50, 36 and 30 K/s in 3 s of cooling time, which shows that the cooling rate decreases with the increase in distance from the friction interface. At the end of friction stage, the interface materials cool very rapidly due to the flash formation and heat dissipation into the surrounding materials.

The measured peak temperatures at the different measured locations are listed in Table 7. Temperature at initial distance of 2.5 mm from interface shows the highest temperature. It can be inferred that the peak temperature and cooling rate may be little higher in the friction interface region. The interface temperature cannot be measured directly by thermocouples because of the severe plastic deformation at the friction interface. However, the peak temperature at the friction interface is calculated approximately by heat transfer analytical methods. As reported in Ref. [30], based on a one-dimensional transient-heat-conduction analysis, the temperature at different distances (d_{axial}) from interface as a function of time (t_f) is

$$T\left(d_{\text{axial}},t_{\text{f}}\right)=T_0+2q_{\text{f}}\sqrt{\frac{t_{\text{f}}}{k\rho c_p\pi}}\exp\left(-\frac{\rho c_p d_{\text{axial}}{}^2}{4kt}\right)-\frac{q_{\text{f}}d_{\text{axial}}}{k}\left[1-\text{erf}\left(\frac{d_{\text{axial}}}{2}\sqrt{\frac{\rho c_p}{kt_{\text{f}}}}\right)\right] \quad (7)$$

where T_0, q_f, k, and erf are respectively the room temperature, average heat input, thermal conductivity, and error function. Here, k is 188 W/(m·K) for AA2024. The average heat input in the CDFW as reported by LI et al [22] is expressed as

$$q_{\text{f}}=\frac{2}{3}\mu P_{\text{N}}\omega r \quad (8)$$

where μ, P_N, ω and r are the average friction coefficient, normal pressure, angle velocity and radius of bar, respectively. Herein, the average friction coefficient of 0.12 is used according to the Ref. [31]. The values for P_N, ω and r are 40 MPa, 230 r/s and 6 mm, respectively. To ensure the accuracy of Eq. (7), initially, the temperature calculated by Eq. (7) at four different distances are compared with the measured results from the thermocouples. The results show a good agreement between the analytical and measured values. On this basis, interfacial temperature at the d_{axial}=0 after friction time of 8 s is estimated to be 769 K. Owing to the temperature rise of 10−24 K caused by plastic deformation, the peak temperature at the interface can be estimated as 779−794 K, which is very close to or even higher than the ternary eutectic temperature 780 K of Al−Cu phase diagram [32].

Table 7 Peak temperature at different distances from friction interface

Initial (final) distance from interface/mm	Measured peak temperature/K	Calculated peak temperature/K
7 (5.5)	652±11	658
5 (3.5)	698±5	687
3 (1.6)	755±8	720
2.5 (0.1)	776±4	725
0	T_{int}>776	779−794

T_{int} represents the interface temperature

3.2.2 Microstructures in weld zone

The typical joint appearance of CDFWed joint of AA2024 at P_f=40 MPa, t_f=8 s and P_u=110 MPa is shown in Fig. 6. It is seen that the cracking phenomenon occurred in the flash, which is attributed to that the low ductility materials are extruded out rapidly under upset pressure. Although the crack may propagate to the flash root, no crack phenomenon is observed at the friction interface. As shown in Fig. 6(b), the cross-section of joint clearly exhibits different microstructural characteristic zones as well as that of joints for other Al

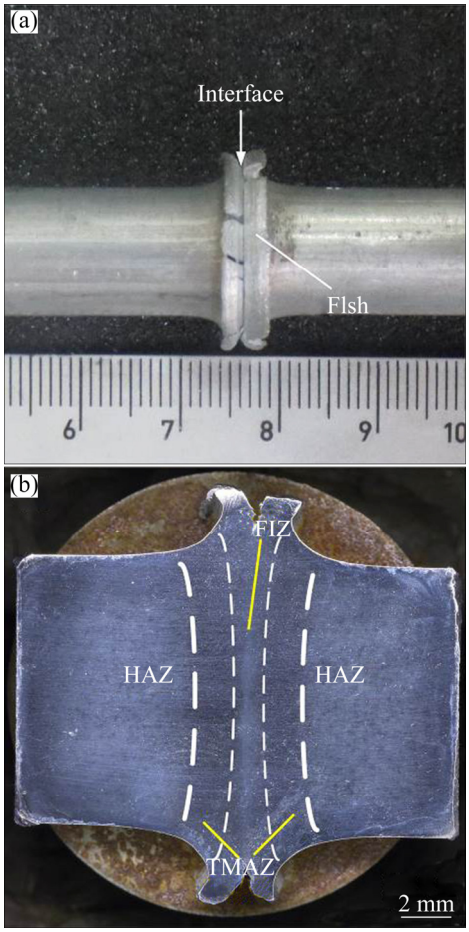

Fig. 6 Typical appearance of friction welded AA2024 joint: (a) Joint; (b) Cross-section

alloys [9−11]: friction interface zone (FIZ), thermo-mechanically affected zone (TMAZ), and heat affected zone (HAZ). Due to the high thermal conductivity of Al alloys, the areas of plastic deformation zone and HAZ are wider than those of joint of other metals [33]. In addition, it is also found that the asymmetric flash is exhibited at both sides of friction interface, which indicates that two Al alloy bars experience different thermomechanical conditions during CDFW.

The typical microstructures in different weld zones are shown in Fig. 7. The coupled influences of high temperature and severe plastic deformation result in the recrystallization, which causes a significant grain refinement in the FIZ (Fig. 7(a)). It is seen that the matrix grain in the FIZ is equiaxed and refined as shown in Fig. 7(a). The particles disperse more evenly along grain boundaries compared with those in the base metal (BM). As a result, the joint efficiency of interface has been improved owing to the grain refining and the second phase strengthening. In TMAZ, some fine grains are observed while most of them retain the size and morphology as those in BM. This shows that the grain refinement is limited in TMAZ due to the insufficient recrystallization caused by relatively low temperature. The matrix grains in TMAZ are deformed severely under the effects of the plastic flow. Figures 7(c, d, e) clearly show the direction of plastic deformation in the different regions of TMAZ. A large number of flow lines form in TMAZ, which are caused by the rearrangement of strengthening particles. In addition, the matrix grains in HAZ are coarsened slightly owing to the thermal influence.

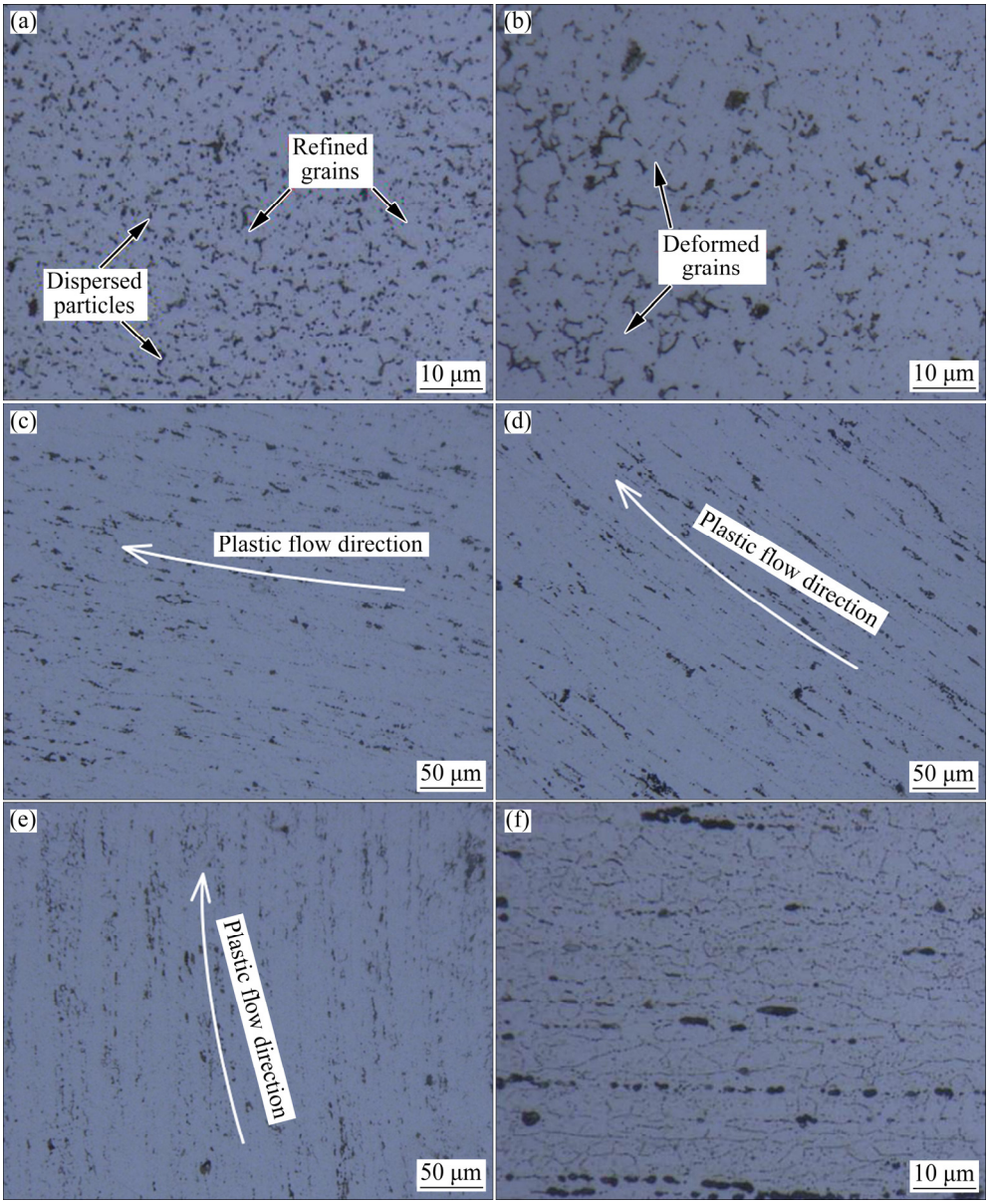

Fig. 7 Typical microstructures in different zones of joint: (a) WZ center; (b) TMAZ center; (c) Flow line at center of TMAZ; (d) Flow line at 1/2 radius of TMAZ; (e) Flow line at periphery of TMAZ; (F) HAZ

The precipitated particles play a predominant role in improving mechanical properties of joint for hard aluminum alloys [34]. Figure 8 shows the SEM images of FIZ, TMAZ and HAZ. As presented in Figs. 8(a, b, c), the precipitated particles show three different microstructural morphologies: ultra-fine dispersed particles in FIZ, elongated and coarsened particles in TMAZ and round particles in HAZ. Compared to BM, the ultra-fine particles indicate that the dissolution and re-precipitation of strengthening phases occur at the friction interface. As proved previously, the microstructure in FIZ undergoes the peak temperature higher than 776 K, which is close to or even high than the ternary eutectoid temperature. Moreover, the actual ternary temperature at non-equilibrium process may be lower than 780 K because the materials in FIZ undergo the high interface stress driving from external force [35]. As a result, the combined effects of high temperature and plastic flow during process result in the dissolution of the original precipitates: $\theta \rightarrow \alpha$(Al). At the end of friction stage, the following reaction process may occur: $\theta \rightarrow \alpha$(Al) + L in the local region of FIZ, accompanied by the ternary invariant reaction for Al−Cu−Mg: $L \rightarrow \alpha$(Al)+θ+S. The results of EDS analysis identify the precipitates as Al_2Cu (θ) and Al_2CuMg (S), as listed in Table 8. TMAZ adjacent to the friction interface undergoes the relatively high temperature, which is lower than that in FIZ. According to the temperature analysis above, the temperature range in TMAZ was estimated as 673−743 K. As pointed by yellow circle in Fig. 8(b), only a few particles may experience the process of dissolution and re-precipitation with high temperature and plastic flow. However, plenty of particles in TMAZ retain their original morphology and size in BM owing to the existing temperature gradient from FIZ to TMAZ. Under the effect of high strain rate plastic flow, these precipitates are elongated along the direction of plastic flow. Besides, as proved by EDS results in Table 8, there is (Fe,Mn)Al_3 or (Mn,Fe)Al_6 phases in TMAZ, which can reduce the ductility of aluminum alloy [36,37]. In contrast, there is minimal dissolution of the precipitates in HAZ during welding. It is seen that the precipitation is coarse as well as that in BM, as presented in Fig. 8(c). Processing temperature of HAZ is estimated in the range of 543−663 K, which is close to the dissolution or coarsening temperature of precipitates [38].

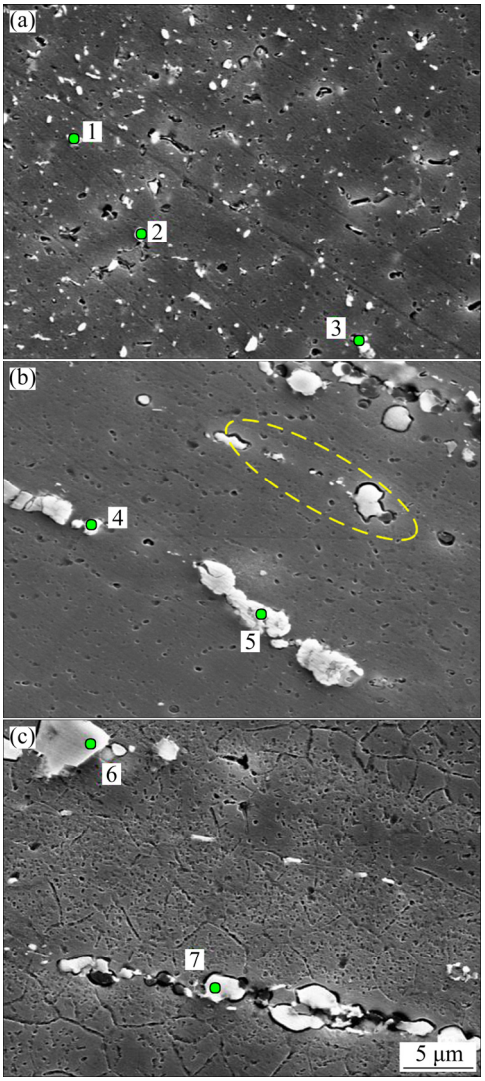

Fig. 8 SEM images of joint in different zones: (a) FIZ; (b) TMAZ; (c) HAZ

Table 8 EDS analysis results at different positions in Fig. 8

Position No.	Content/at.%					Possible phase
	Al	Cu	Mg	Fe	Mn	
1	61.82	24.25	13.9	−	−	S+θ
2	64.15	2172	14.11	−	−	S+θ
3	78.80	14.78	6.42	−	−	S+θ
4	80.21	8.96	−	7.05	3.75	θ+(Fe,Mn)$Al_{3/6}$
5	68.51	23.72	−	6.10	1.67	θ+(Fe,Mn)$Al_{3/6}$
6	67.66	32.34	−	−	−	θ
7	75.53	21.25	4.22	−	−	θ

3.2.3 Microhardness measurement

Microhardness usually reflects the localized resistance to plastic deformation of microstructure, which is mainly affected by the refined grain strengthening and second phase strengthening [30]. Figure 9 shows the micro-hardness distribution at the cross-section of optimal joint. The value of microhardness in the weld is in the range of HV (121±3) to (149±2). No softening region is presented in the CDFWed joint at optimal welding parameters. The microhardness in the weld exhibited obvious asymmetric distribution, which indicates that two bars experienced different thermomechanical conditions.

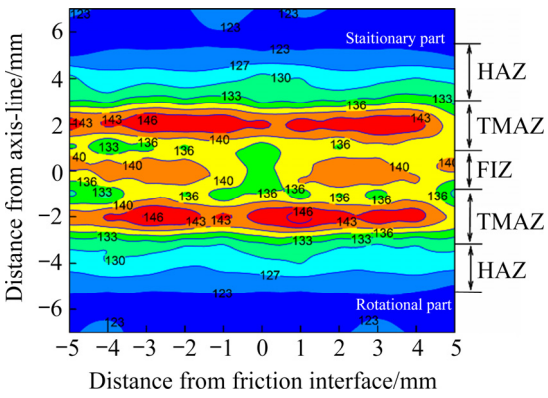

Fig. 9 Microhardness distribution of welded joint at optimal welding parameters

The maximum microhardness appears in the region of TMAZ. With the increase of distance from interface, microhardness first increases from FIZ microhardness of HV (138±4) to the maximum of HV (149±2) in TMAZ, and then gradually reaches the BM hardness value of HV (121±3). It is also seen that the microhardness along the friction interface is non-uniform, which shows a relatively low value at the center of interface. This can be attributed to the non-uniformity of microhardness due to the distribution of temperature and plastic deformation. As investigated numerically by HYNES et al [33], the dynamic recrystallization of microstructure at the radius area was more sufficient than that at the center area. In addition, the maximum heat generation is produced at somewhere between (1/2)*R* and (2/3)*R* due to the uneven distributed friction pressure [34]. It is reasonable that the higher friction heating with severe plastic deformation at the radius area results in the larger grain refinement effect.

The higher microhardness in FIZ compared with that in BM can be attributed to the combined effects of grain refinement and precipitated particles. Although the size of re-precipitated strengthening particles in FIZ is smaller compared with that in TMAZ, the volume fraction of strengthening phases is reduced extensively due to the high cooling rate in FIZ. Besides, the maximum microhardness appearing in TMAZ can be related to the presence of refined grains and work hardening effects of plastic deformation. The microhardness in HAZ is slightly higher than that in BM. This may be related to the re-precipitation of strengthening phases, because the cooling rates are relatively low in HAZ.

3.2.4 Fracture surface

The tensile strength of joint at optimal welding parameters reaches 92% of that of BM. After tensile testing, the fractured position of tensile specimen is shown in Fig. 10. The fractured position is presented in FIZ and TMAZ. Most of fractured areas distribute in TMAZ, indicating weak bonding strength in the TMAZ compared with BM and FIZ. This may be attributed to the fact that TMAZ experiences high temperatures for causing coarsening of original strengthening phases or precipitating of any brittle phases. Figure 11 shows the

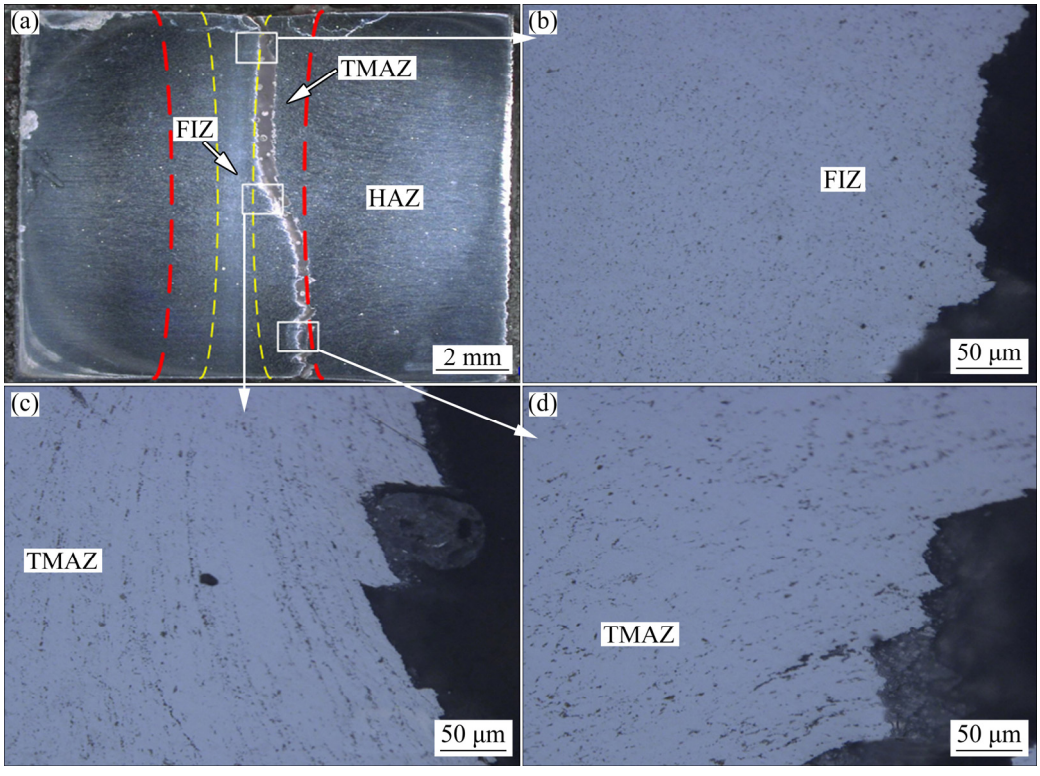

Fig. 10 OM images of fractured position of joint at optimal welding parameters after tensile testing

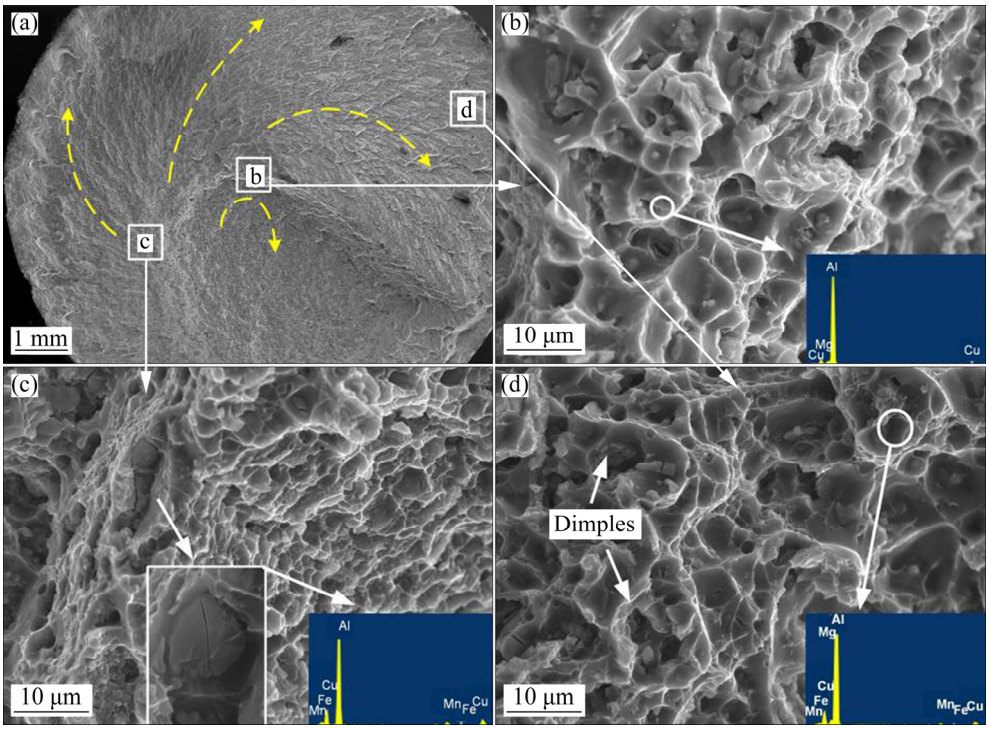

Fig. 11 SEM images of fracture surface of joint at optimal welding parameters

SEM images of fracture surface of joint at optimal welding parameters. It can be observed from the fracture pattern direction in Fig. 11(a) that the crack initiates from the center of TMAZ. Figures 11(b), (c) and (d) show the surface morphologies in different regions of fractured surface, respectively. As is seen, there are a lot of dimples with various depths and sizes. This phenomenon shows that the ductile fracture is the predominant facture mode. Comparing the dimple size with that in other regions, it is found that the number of dimples increases as the dimple size decreases with fine grain. The position of strengthening phases can be the sites of crack nucleation as proved by the EDS results. As shown in Fig. 11(c), the trans-granular cracks originate from the brittle particle, which are in the internal region of dimple. The results of EDS indicated that the possible brittle phase may be the (Fe,Mn)Al_3 phase, which usually deteriorates the joint ductile.

4 Conclusions

(1) A sound joint of AA2024 is obtained using CDFW, with the highest joint efficiency of 92% at optimal welding parameters. Friction pressure is the most significant factor affecting the tensile strength of CDFWed joints of AA2024. Combination of moderate friction pressure (40 MPa), less friction time (4−8 s) and higher upset pressure (90−110 MPa) is recommended for CDFW of 12 mm-diameter bars of AA2024.

(2) Peak temperature at the friction interface is estimated in the range of 779−794 K using a one-dimensional-heat-conduction analysis. The temperature increase at the beginning of upset stage is estimated as 9−24 K, which is due to the plastic deformation work, accompanied with the sharp increase of axial shortening length.

(3) Owing to the sufficient dynamic recrystallization, refined grains are observed in FIZ. The grain refinement is limited in the thermo-mechanically affected zone, where most of matrix grains are deformed severely. The obvious flow lines are observed in TMAZ due to the rearrangement of strengthening phases.

(4) The presence of refined grains and work hardening effects of plastic deformation result in the maximum microhardness in TMAZ. The extensive dissolution and limited re-precipitation of strengthening phases make the microhardness in FIZ lower than TMAZ, but higher than the BM. Plenty of dimples distributed on the fracture surface prove a predominantly ductile fracture mode.

References

[1] BERGMANN J P, GRATZEL M, SCHURER R, REGENSBURG A, WEIGL M. Advances and potentials in friction stir welding of aluminum alloys [J]. Key Engineering Materials, 2016, 710: 137−142.

[2] GU J L, BAI J, DING J L, WILLIAMS S, WANG L, LIU K. STEWART W, WANG Li-min, LIU K. Design and cracking susceptibility of additively manufactured Al−Cu−Mg alloys with tandem wires and pulsed arc [J]. Journal of Materials Processing

Technology, 2018, 262: 210−220.

[3] RAO S R K, REDDY G M, KAMARAJ M, RAO K P. Grain refinement through arc manipulation techniques in Al−Cu alloy GTA welds [J]. Materials Science and Engineering A, 2005, 404(1−2): 227−234.

[4] YAN J, ZENG X Y, GAO M, LAI J, LIN T. Effect of welding wires on microstructure and mechanical properties of 2A12 aluminum alloy in CO_2 laser-MIG hybrid welding [J]. Apply Surface Science, 2009, 255(16): 7307−7313.

[5] BALASUBRABNABIAN V, RAVISANKAR V, REDDY G M. Effect of pulsed current welding on fatigue behaviour of high strength aluminum alloy joints [J]. Material & Design, 2008, 29(2): 492−500.

[6] MA H, QIN G L, GENG P H, LI F, FU B L, MENG X M. Microstructure characterization and properties of carbon steel to stainless steel dissimilar metal joint made by friction welding [J]. Material & Design, 2015, 86: 587−597.

[7] CHAMANFAR A, JAHAZI M, CORMIER J. A review on inertia and linear friction welding of Ni-based superalloys [J]. Metallurgical Material Transaction A, 2015, 46(4): 1639−1669.

[8] LIENERT T J, BAESLACK W A, RINGNALDA J, FRASER H L. Inertia-friction welding of SiC-reinforced 8009 aluminium [J]. Journal of Material Science, 1996, 31(8): 2149−2157.

[9] KIMURA M, CHOJI M, KUSAAKAL M, SEO K, FUJI A. Effect of friction welding conditions on mechanical properties of A5052 aluminum alloy friction welded joint [J]. Science Technology of Welding and Joining, 2006, 11(2): 209−215.

[10] KIMURA M, KUSAAKAL M, SEO K, FUJI A. Joining phenomena during friction stage of AA7075-T6 aluminum alloy friction weld [J]. Science Technology of Welding and Joining, 2005, 10(3): 378−383.

[11] RAFI H K, RAM G D J, PHANIKUMAR G, RAO K P. Microstructure and tensile properties of friction welded aluminum alloy AA7075-T6 [J]. Material & Design 2010, 31(5): 2375−2380.

[12] YAMAMOTO Y, OCHI H, SAWAI T, YAMAGUCHI H, OGAWA K. Fatigue strength of friction-welded 6061 aluminum alloy joints [J]. Material Transaction 2007, 48(11): 2909−2913.

[13] SAHIN M, BALASUBRAMANIAN N, MISIRLI C, AKATA H E, CAN Y, OZEL K. On properties at interfaces of friction welded near-nanostructured Al 5083 alloys [J]. International Journal of Advanced Manufacturing Technology, 2012, 61(9−12): 935−943.

[14] DONATI L, TROIANI E, PROLI P, TOMESANI L. FEM analysis and experimental validation of friction welding process of 6xxx alloys for the prediction of welding quality [J]. Material Today: Proceedings, 2015, 2(10): 5045−5054.

[15] SINGH S K, CHATTOPADHYAY K, PHANIKUMAR G, DUTTA P. Experimental and numerical studies on friction welding of thixocast A356 aluminum alloy [J]. Acta Material, 2014, 73: 177−185.

[16] SINGH S K, CHATTOPADHYAY K, DUTTA P. Friction welding of thixocast A356 aluminium alloy [J]. Solid State Phenomena, 2013, 192−193: 305−310.

[17] DARSIN M, SUTJAHJONO H, HADI A. Mechanical properties and micro structure of aluminum alloys [Al−Mg−Si] as results of variation time in friction welding [C]//The 13th International Conference on QIR (Quality in Research). Yogyakarta, Indonesia, 2013: 249−254.

[18] WANG X Z, WANG L P, HAN L J. Continuous drive friction welding process of 6063-T6 aluminum alloy tube [J]. Development and Application of Materials, 2012, 27(3): 20−22.

[19] DAI A L. Structure and properties of friction welded joints of spray forming 7055 aluminum alloy [J]. Journal of Materials Science and Engineering, 2014, 32(2): 242−247.

[20] TAYLOR J, ANDERSON V L, MCLEAN R A. Design of experiments: A realistic approach [J]. Applied Statistics, 1974, 25(1): 55−71.

[21] MAHENDIRAN S, RAMANUJAM R, MOHANAVEL V, RAVIKUMAR M M, MADHAN G, VINOTHKUMAR P. Parametric optimisation of friction welded 17-4 PH SS alloy using Taguchi techniques [J]. Progress in Industrial Ecology, 2018, 12(1−2): 3−13.

[22] LI W Y, VAIRIS A, PREUSS M, MA T J. Linear and rotary friction welding review [J]. International Material Review, 2016, 61(2): 71−100.

[23] LAKSHMINARAYANAN A K, BALASUBRAMANIAN V. Process parameters optimization for friction stir welding of RDE-40 aluminum alloy using Taguchi technique [J]. Transactions of Nonferrous Metals Society of China, 2008, 18(3): 548−554.

[24] VIJIAN P, ARUNACHALAM V P. Optimization of squeeze casting process parameters using Taguchi analysis [J]. International Journal of Advanced Manufacturing Technology, 2007, 33(11−12): 1122−1127.

[25] GOETZ R L, SEMIATIN S L. The adiabatic correction factor for deformation heating during the uniaxial compression test [J]. Journal of Material Engineering and Performance 2001, 10(6): 710−717.

[26] HAMILTON C, DYMEK S, SOMMERS A. A thermal model of friction stir welding in aluminum alloys [J]. International Journal of Machine Tools and Manufacture, 2008, 48(10): 1120−1130.

[27] MEYER M, PONTIKIS V. Computer simulation in materials science: Interatomic potentials, simulation techniques and applications [M]. Kluwer: Springer Science & Business Media, 2012.

[28] MIRZADEH H. Simple physically-based constitutive equations for hot deformation of 2024 and 7075 aluminum alloys [J]. Transactions of Nonferrous Metals Society of China, 2015, 25(5): 1614−1618.

[29] GTANT B, PREUSS M, WITHERS P J, BAXTER G, ROWLSON M. Finite element process modelling of inertia friction welding advanced nickel-based superalloy [J]. Material Science and Engineering A, 2009, 513−514: 366−375.

[30] CHAMANFAR A, JAHAZI M, GHOLIPOUR J, WANJARA P, YUE S. Mechanical property and microstructure of linear friction welded Waspaloy [J]. Metallurgical and Material Transaction A, 2011, 42(3): 729−744.

[31] AWANG M, MUCINO V H, FENG Z, DAVID S A. Thermo-mechanical modeling of friction stir spot welding (FSSW) process: Use of an explicit adaptive meshing scheme [R]//SAE Technical Paper, 2005.

[32] LIANG S M, SCHMID F R. Thermodynamic assessment of the Al−Cu−Zn system. Part II: Al−Cu binary system [J]. Calphad, 2015, 51: 252−260.

[33] HYNES N R J, VELU P S. Effect of rotational speed on Ti−6Al−4V−AA 6061 friction welded joints [J]. Journal of Manufacturing Processes, 2018, 32: 288−297.

[34] CHENG T, JIA Z H, WENG Y Y, HAO L L, LIU Q. Effects of Sn/In additions on natural and artificial ageing of Al−Mg−Si alloys [J]. Materials Science and Technology, 2018, 34: 2136−2144.

[35] NIE L F, ZHANG L W, ZHU Z, XU W. Microstructure evolution modeling of FGH96 superalloy during inertia friction welding process [J]. Finite Element in Analysis and Design, 2014, 80: 63−68.

[36] QIU R F, IWAMOTO C, SATONAKA S. Interfacial reaction layer in resistance spot welded joint between aluminum alloy and austenitic stainless steel [J]. Material Science and Technology, 2010, 26(2): 243−246.

[37] SHEN J J, SUHUDDIN U F H, CARDILLO M E B, SANTOS J F. Eutectic structures in friction spot welding joint of aluminum alloy to copper [J]. Apply Physics Letters, 2014, 104(19): 191901−191904.

[38] RECORD J H, COVIANGTON J L, NELSON T W, SORENSEN C D, WEBB B W. Fundamental characterization of friction stir welding [C]//Proc 5th Int Symp on Friction Stir Welding. Metz: TWI Ltd, 2004.

航空用铝合金 2024 摩擦焊接工艺参数优化及显微组织

耿培皓[1,2]，秦国梁[1,2]，周 军[3]，李长安[1,2]

1. 山东大学 材料液固结构演变与加工教育部重点实验室，济南 250061；
2. 山东大学 材料连接技术研究所，济南 250061；
3. 机械科学研究院 哈尔滨焊接研究所，哈尔滨 150028

摘 要：开展航空用铝合金 2024 的连续驱动摩擦焊工艺优化试验，并表征焊接接头的显微组织演变。结果表明，摩擦压力是影响焊接接头抗拉强度的最显著因素，而采用适中的摩擦压力匹配较短的摩擦时间和较高的顶锻压力更易获取较高抗拉强度的接头。采用田口分析优化后的焊接工艺参数，焊后接头抗拉强度能够达到原始母材的 92%。通过解析求解得到优化焊接工艺参数下焊接过程中摩擦界面的峰值温度处于 779−794 K，与试验测量结果吻合良好。由于高温和塑性变形的影响，摩擦界面的晶粒发生动态再结晶后尺寸明显细化。热影响区的晶粒细化有限，大部分原始晶粒受塑性流动影响发生变形。在摩擦阶段由于界面区域原始强化相发生固溶，且在随后冷却中二次析出不完全，最终导致摩擦界面的显微硬度降低。

关键词：AA2024 合金；连续驱动摩擦焊；田口分析；显微组织演变；力学性能

(Edited by Xiang-qun LI)